MNRAS **000**, 1–11 (2020) Preprint 17 June 2020 Compiled using MNRAS LATEX style file v3.0

Fe III emission in quasars: evidence for a dense turbulent medium

Matthew J. Temple,[1]★ Gary J. Ferland,[2] Amy L. Rankine,[1] Paul C. Hewett,[1] N. R. Badnell,[3] Connor P. Ballance,[4] Giulio Del Zanna,[5] and Roger P. Dufresne[5]

[1] *Institute of Astronomy, University of Cambridge, Madingley Road, Cambridge CB3 0HA, UK*
[2] *Department of Physics and Astronomy, The University of Kentucky, Lexington, KY 40506, USA*
[3] *Department of Physics, University of Strathclyde, Glasgow, G4 0NG, UK*
[4] *Centre of Theoretical Atomic, Molecular and Optical Physics, Queen's University Belfast, Belfast BT7 1NN, UK*
[5] *Department of Applied Mathematics and Theoretical Physics, University of Cambridge, Wilberforce Road, Cambridge CB3 0WA, UK*

Accepted 2020 June 12. Received 2020 June 12; in original form 2020 February 12

ABSTRACT

Recent improvements to atomic energy-level data allow, for the first time, accurate predictions to be made for the Fe III line emission strengths in the spectra of luminous, $L_{\rm bol} \simeq 10^{46} - 10^{48}\,{\rm erg\,s^{-1}}$, Active Galactic Nuclei. The Fe III emitting gas must be primarily photoionized, consistent with observations of line reverberation. We use CLOUDY models exploring a wide range of parameter space, together with ≃26,000 rest-frame ultraviolet spectra from the Sloan Digital Sky Survey, to constrain the physical conditions of the line emitting gas. The observed Fe III emission is best accounted for by dense ($n_{\boldsymbol{H}} \simeq 10^{14}\,{\rm cm^{-3}}$) gas which is microturbulent, leading to smaller line optical depths and fluorescent excitation. Such high density gas appears to be present in the central regions of the majority of luminous quasars. Using our favoured model, we present theoretical predictions for the relative strengths of the Fe III UV34 $\lambda\lambda$1895,1914,1926 multiplet. This multiplet is blended with the Si III] λ1892 and C III] λ1909 emission lines and an accurate subtraction of UV34 is essential when using these lines to infer information about the physics of the broad line region in quasars.

Key words: atomic data – plasmas – quasars: general – quasars: emission lines

1 INTRODUCTION

Iron lines have long been recognised as an important component in the spectra of active galactic nuclei (AGN) and quasars. For example, emission from the Fe II ion has been identified as one of the major sources of cooling in the broad line region (BLR; Wills et al. 1985) and an important contributor to the observed population variance within optical quasar spectra (the so-called 'eigenvector 1'; Boroson & Green 1992). There is now an extensive literature investigating the properties of the low-ionization (16.2 eV) Fe II emission in quasars and AGN. Recent results of reverberation-mapping campaigns indicate that the Fe II emission originates in gas at distances comparable to, or larger than, the gas responsible for much of the hydrogen Balmer emission in both low and high luminosity AGN (e.g. Hu et al. 2015; Zhang et al. 2019).

Empirical iron templates such as those provided by Vestergaard & Wilkes (2001) have also identified Fe III (ionization potential 30.6 eV) as a significant source of emission, which needs to be accounted for when modelling emission lines such as the C III] λ1909 blend. However, until recently the electronic energy structure of the Fe^{2+} ion was poorly known and so theoretical predictions for the Fe III line ratios and strengths were not accurate. Within the past few years, work by Badnell & Ballance (2014) has produced improved atomic data for Fe III which, for the first time, allows predictions to be made for the full emission-line spectrum of this ion (Laha et al. 2017).

Previous observational studies of Fe III have focused on the complex of lines at ∼2075 Å, which is relatively isolated and measurements are thus relatively straightforward. Fian et al. (2018) find evidence that the complex of Fe III lines at $\lambda\lambda$2039-2113 is strongly microlensed in a sample of 11 gravitationally lensed high luminosity quasars, suggesting the line emitting region is no more than a few light days across. At lower luminosity, Mediavilla et al. (2018, 2019) suggest that the Fe III in NGC 5548 reverberates with a time scale of around three days, which is shorter than the predicted time

★ E-mail: mtemple@ast.cam.ac.uk

of 10-20 days estimated for Fe II reverberation in the same object (Hu et al. 2015). Thus, over an extended range of luminosities, investigation of Fe III emission can probe the conditions of gas in quasars and AGN closer to the central ionizing source than is the case for Fe II emission.

The structure of this paper is as follows. In Section 2 we discuss the theory of the Fe^{2+} ion and constrain its excitation mechanism using existing high signal-to-noise ratio composite spectra in the rest-frame ultraviolet. Spectra from the fourteenth data release of the Sloan Digital Sky Survey (SDSS DR14Q; Pâris et al. 2018) provide the basis for an investigation of the statistical properties of Fe III emission in the population of high luminosity, $\log_{10}(L_{\rm bol}/\,{\rm erg\,s^{-1}}) \simeq 46.5$, quasars with redshifts $1.2 < z < 2.3$. In Section 3 we outline the selection of a sample of such objects from the DR14Q catalogue to investigate the Fe III emission across the quasar population. Initial investigation of the sample is used to demonstrate the presence of Fe III emission with significant equivalent width at wavelengths ≃1850-2150 Å. The observation is used to motivate additional theoretical investigation in Section 4, where we present further results of Cloudy models. The particular focus is to place constraints on the temperature, density and turbulence of the Fe III emitting gas. In Section 5 we then check the consistency of our preferred model with a more involved consideration of the Fe III emission properties using the full quasar sample. The implications for our understanding of quasar broad-line regions form the basis for the discussion in Section 6. The paper concludes with a short summary of the main results in Section 7.

We assume a flat ΛCDM cosmology throughout this work, with $\Omega_m = 0.3$, $\Omega_\Lambda = 0.7$, and $H_0 = 70\,{\rm km\,s^{-1}\ Mpc^{-1}}$. All emission lines are identified with their wavelengths in vacuum in units of Ångströms.

2 FORMATION OF Fe III LINES IN AGN

Spectral calculations are performed using version 17.02 of Cloudy, last described by Ferland et al. (2017). Figure 1 shows the Fe III model now implemented in Cloudy. Data are largely from Badnell & Ballance (2014) with experimental energies from the National Institute of Standards and Technology (NIST) atomic spectra database (Kramida et al. 2018) adopted where possible. Previous work on the Fe III ion is summarized by Badnell & Ballance (2014).

This paper centres on Fe III UV34 (as defined by Moore 1952) at $\lambda\lambda 1895, 1914, 1926$ resulting from the septet transition indicated in Fig. 1 and also the strongest Fe III multiplet indicated in the Vestergaard & Wilkes (2001) template. According to NIST the next higher septet is ^7D at 147 000 wavenumbers, a level not included in Badnell & Ballance (2014). Little is known about the emission properties of Fe III from the dense gas found near the centres of AGN and we begin with some fundamental considerations.

Lines can form via two processes, photoionization or collisional ionization. The key difference is in the gas kinetic temperature, with photoionized gas having a temperature set by energy balance, generally around 10^4 K (Osterbrock & Ferland 2006), while the gas kinetic temperature is near the ionization temperature of the ion in collisional equilibrium, around $10^{4.5}$ K for Fe^{2+} (Lykins et al. 2013).

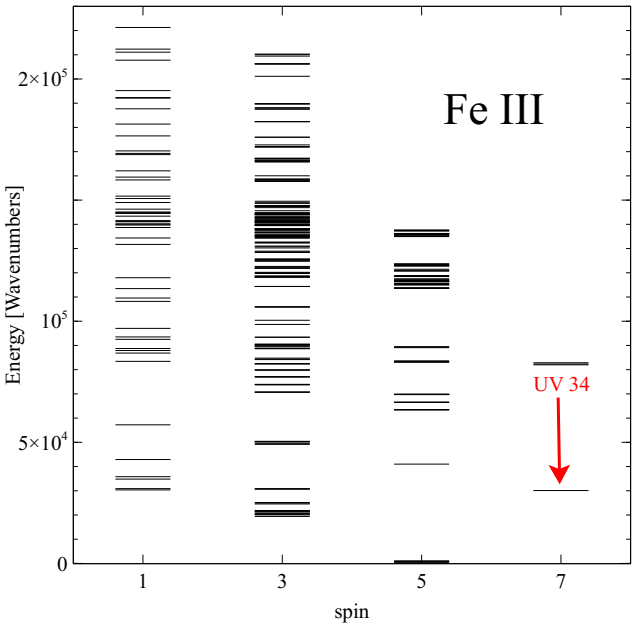

Figure 1. The Fe III model now implemented in Cloudy. The UV34 transition studied in this paper is indicated.

Figure 2 compares the resulting emission spectra of a pure Fe^{2+} gas with a density of $n_e = 10^{11}\,{\rm cm^{-3}}$. Both spectra are from a 'unit cell', a cubic-centimetre of gas, to ensure that the spectrum is not affected by radiative transfer effects. An incident radiation field is not included in the collisional case so as to ensure a pure collisional model.

The differences in the gas kinetic temperature for the two cases result in spectra of very different form. While the UV34 multiplet is strongest in both cases, electron collisions in the much warmer gas of the collisional-ionization model excite higher-energy levels, producing emission at shorter ultraviolet wavelengths. In particular, there is significant emission just below 0.1 μm. The photoionization case is much cooler so the gas is ≃3 dex less emissive (the independent axis in each panel can be compared directly) and short wavelength transitions are even weaker.

The difference in predicted Fe III emission strength below 1000 Å is such that existing ultraviolet spectra of luminous quasars can discriminate between a collisional and photoionization origin for the iron emission. The composite quasar spectrum of Stevans et al. (2014, their fig. 5), constructed using *Hubble Space Telescope*-Cosmic Origins Spectrograph spectra of 159 AGN at $z < 1.5$, possesses both high signal-to-noise ratio (S/N) and high resolution (≃7500). The rest-frame spectrum from the relatively low redshift AGN contributing to the composite is not significantly affected by Lyman absorption from the inter-galactic medium.

Stevans et al. (2014) identify Fe III emission at 1125 Å, as predicted by both our photoionized and collisionally ionized models. The quality of the composite spectrum is such that weak emission features with equivalent widths of only a few Ångströms are detectable. Examination of their composite, however, confirms there is no evidence for Fe III emission in the 800-900 Å region, where we would expect to see strong

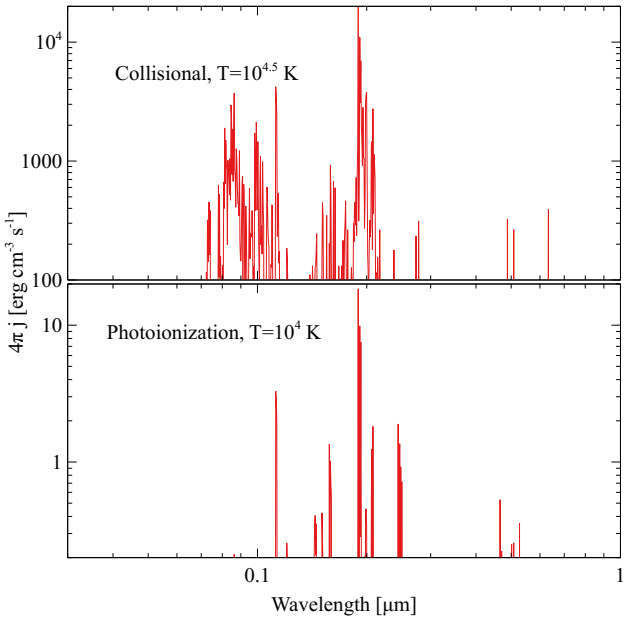

Figure 2. The Fe III emission spectrum for typical photoionization (bottom) and collisional ionization (top) temperatures. The gas has only Fe^{2+} and an electron density of 10^{11} cm^{-3}. The spectrum is from a unit cell in which the gas experiences only collisional excitation. The dynamic range of the y-axis is adjusted to only show lines brighter than one per cent of UV34.

emission if the Fe III emitting gas was collisionally excited (cf. our Fig. 2).

The first conclusion of the paper is, therefore, that there is no evidence for detectable collisionally-ionized Fe III emission in the ultraviolet spectra of luminous quasars and a photoionized origin for the Fe III emission is strongly favoured. This is consistent with the reverberation of Fe III in response to continuum variation reported by Mediavilla et al. (2018, 2019).

While collisional-ionization can be ruled out as the physical process responsible for the observed Fe III emission, there is an apparent tension between the low emissivity of the Cloudy photoionization model and the strong Fe III UV34 emission seen in the Vestergaard & Wilkes (2001) iron emission template. More quantitative measures of Fe III emission in the population of luminous quasars can constrain the Cloudy model predictions. In the next section, following the definition of the quasar sample to be used, we therefore make an initial measurement of the strength of Fe III UV34 and λ2075 emission to guide the theoretical investigation presented in Section 4.

3 OBSERVATIONAL QUASAR DATA

3.1 Quasar sample

To characterize the Fe III emission in the rest-frame near-ultraviolet spectra of the luminous quasar population we use the quasar catalogue from the fourteenth data release of the SDSS (DR14Q; Pâris et al. 2018). Selecting objects with redshifts in the range $1.20 < z < 2.30$ provides rest-frame wavelength coverage over the interval 1700-3000 Å which includes the C III] λ1909 blend, Mg II λ2800 emission and the complex of Fe III lines at ~2075 Å. The reliability of emission line measurements is poor for spectra of the fainter quasars in the DR14Q catalogue and a minimum S/N of 10 per 69 km s^{-1} pixel over the wavelength interval 1700-3000 Å is imposed.

The resulting sample consists of 26 501 quasars with redshifts $1.20 < z < 2.30$ and luminosities $10^{45.8} < L_{\rm bol} < 10^{48.1}$ erg s^{-1} . The median luminosity of the sample is $L_{\rm bol} = 10^{46.4}$ erg s^{-1} .

For comparison with later results, we note that the median luminosity in the sample corresponds to C IV emission line lag of 73^{+21}_{-16} light-days behind the continuum, assuming the bolometric correction $L_{\rm bol} = 3.81 \times L_{1350}$ from Shen et al. (2011) and the luminosity-lag relation from Grier et al. (2019),

$$\log_{10}\left(\frac{R_{\rm CIV}}{\text{light-days}}\right) = 0.92+0.52\times\log_{10}\left(\frac{L_{1350}}{10^{44}\,\text{erg s}^{-1}}\right)\pm0.11 \quad (1)$$

corresponding to a source-cloud separation of 1.89×10^{17} cm for the C IV emitting gas.

3.2 Defining the equivalent width of Fe III emission at 2075 Å

A complex of Fe III transitions blends together to form a feature at ~2075 Å. This feature is relatively isolated, in that it is not blended with emission from other species, and can thus be used to estimate a measure of the strength of Fe III emission in a quasar spectrum.

The equivalent width of this emission feature can be obtained by defining a power-law continuum ($F(\lambda) \propto \lambda^{\alpha}$) and integrating the emission line flux within a specified wavelength range. The median fluxes in two 10 Å-wide intervals, centred on 1975 and 2150 Å, are used to calculate the slope, α, of the continuum. The continuum-subtracted emission is summed over the wavelength interval 2040-2120 Å. Different continuum regions and line-boundaries can be used but the results are not sensitive to the exact wavelengths adopted.

3.3 Directly detectable UV34 emission

The diversity of the morphology of the '1909 Å complex' among luminous quasars is well-established (e.g. Richards et al. 2011, fig. 11). This strong feature consists of the Al III $\lambda\lambda$1855,1863, Si III] λ1892, C III] λ1909 and Fe III UV34 emission lines. In most objects, these lines are blended together and it is hard to disentangle the relative contribution of UV34 from the semi-forbidden lines without additional constraints on the line ratios. However, in objects with narrow emission velocity widths, such as the quasar presented by Graham et al. (1996), the individual lines contributing to the 1909 Å complex deblend and can be directly detected.

Within our sample of quasars it is possible to identify small numbers of objects where the full width at half maximum (FWHM) of Mg II is narrow (< 2800 km s^{-1}) and the C III] λ1909 emission is relatively weak. Figure 3 shows a composite of 44 such quasar spectra. While the definition of their sample differs somewhat, the quasars contributing to our composite are very similar to the extreme 'Population

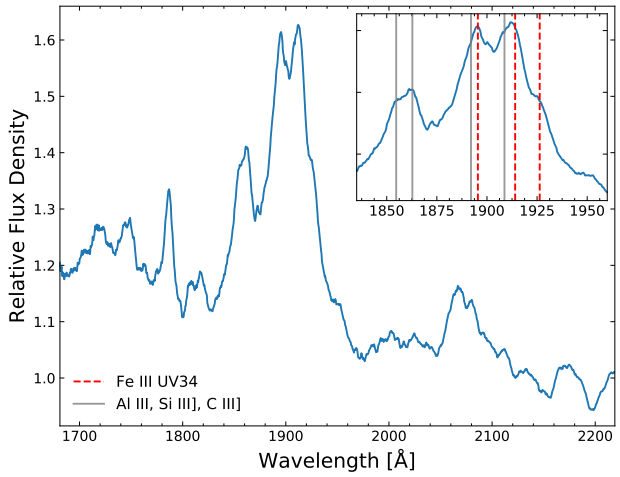

Figure 3. Composite of 44 quasars with narrow Mg II and and weak C III] emission. UV34 emission is directly detectable, and the composite also shows strong Fe III emission at 2075 Å. The spectrum has been smoothed with a 7-pixel (480 km s^{-1}) window to reduce the pixel-to-pixel noise. Inset: the 1909 Å complex, with the wavelengths of the Al III $\lambda\lambda$1855,1863 doublet, C III] λ1909 and Si III] λ1892 lines, and Fe III UV34 multiplet marked.

A' objects discussed by Marziani & Sulentic (2014). Within this composite, we see that the emission doublet from Al III is detectable at the expected wavelengths, and that Si III] λ1892 and C III] λ1909 are very weak. The Fe III UV34 multiplet and Al III $\lambda\lambda$1855,1863 are responsible for the majority of the emission, demonstrating that in at least some quasars Fe III UV34 is present with high, $\gtrsim 5$ Å, equivalent width.

However, for the majority of quasars, the Al III, Fe III UV34, Si III] and C III] lines are blended together. At the typical S/N of available large samples of quasar spectra, such as those from SDSS DR14Q, significant degeneracies exist between measures of the strengths of emission from these species. We therefore require additional constraints on the Fe III emission lines in order to be able to quantify the strength of UV34 across the whole quasar population.

We note in passing that the composite also shows strong Fe II UV191 λ1787 emission, which is indicative of strong continuum fluorescence (i.e. photon pumping, Bottorff et al. 2000), suggesting that this excitation mechanism may also play an important role in the production of Fe III emission.

Before returning to a more extensive investigation of the observational properties of Fe III emission in Section 5, we first make use of the improved atomic data now implemented in Cloudy to produce theoretical predictions for the strengths of these lines emitted from gas under different physical conditions.

4 PHOTOIONIZATION CALCULATIONS

This section presents predictions of the equivalent widths of a number of ultraviolet lines over a broad range of cloud densities and distances from the black hole. Our calculations extend to higher densities than conventional BLR grids (e.g. Baldwin et al. 1995; Korista et al. 1997). We find that the Fe III lines trace especially high density gas that is located close to the black hole. The Fe III energy level diagram (Fig. 1) is highly unusual in that the strongest permitted line, UV34, is a subordinate line that has a different spin than the ground term. Most ultraviolet lines are instead resonance lines and become strongly thermalised at high densities either because of large optical depths or low critical densities. They are weak at high densities as a result. Although the dense clouds do emit in other lines, their contribution is modest compared to emission from lower density components of the BLR. As Fe III emits only very weakly from lower density gas, we find that Fe III is the best tracer of the high density part of the BLR.

4.1 Photoionisation model parameters

We present a first grid of photoionization models assuming that lines within the clouds are broadened only by thermal motions, the usual assumption in BLR modeling, and a second grid including a microturbulence of 300 km s^{-1} which Baldwin et al. (2004) found improved the fit for the Fe II spectrum. The effects of including turbulence on other quasar emission lines are described by Bottorff et al. (2000).

We use the intermediate $L/L_{\rm Edd}$ SED described by Jin et al. (2012). We assume solar abundances and a cloud column density of 10^{23} cm^{-2}, typical assumptions for BLR clouds. With these assumptions the remaining parameters are the flux of ionizing photons striking the cloud, ϕ(H)[cm^{-2} s^{-1}], and the hydrogen density n_H[cm^{-3}]. In Figs. 4 and 5 we vary these parameters over a broad range. Plots similar to these are presented in Baldwin et al. (1995), Korista et al. (1997), and Baldwin et al. (2004).

The following features are presented: C IV λ1549, Al III λ1860, Si III] λ1892, C III] λ1909, C III λ2297, Mg II λ2798, Fe II ultraviolet emission over the interval 2200-2660 Å ('Fe II UV'), and Fe III UV34. All features are shown as equivalent widths in Ångströms expressed relative to the continuum at 1215 Å, and assuming 4π sr coverage of the ionizing source, i.e. a cloud covering factor of unity. In the case of multiplets or blends we predict the total equivalent width. However, the line luminosity or equivalent width depends on the cloud covering factor (Osterbrock & Ferland 2006), and so these predictions need to be multiplied by that factor, which is typically taken to be of order 20 per cent. Adopting this value, an observed Fe III UV34 equivalent width of 5 Å requires a predicted equivalent width of order 25 Å.

The two axes for these contour plots have simple physical meanings. The flux of ionizing photons ϕ(H) is related to the total ionizing photon luminosity, Q(H) [s^{-1}] and the distance of the cloud from the continuum source r by

$$\phi(\mathrm{H}) = \frac{\mathrm{Q(H)}}{4\pi r^2}[\,\mathrm{cm^{-2}\ s^{-1}}\,] \qquad (2)$$

so the vertical axis is related to the cloud separation from the centre, $\phi \propto r^{-2}$ with lower regions representing larger radii. The typical bolometric luminosity of our sample is $10^{46.4}$ erg s^{-1}. This, assuming the middle SED of Jin et al. (2012), corresponds to a photon luminosity of Q(H) = 1.96×10^{56} s^{-1}. For reference, C IV emitting clouds, adopting a lag of 73 light days, have

$$\phi(\mathrm{H}) = 4.36 \times 10^{20} r_{73.6}^{-2}[\,\mathrm{cm^{-2}\ s^{-1}}\,], \qquad (3)$$

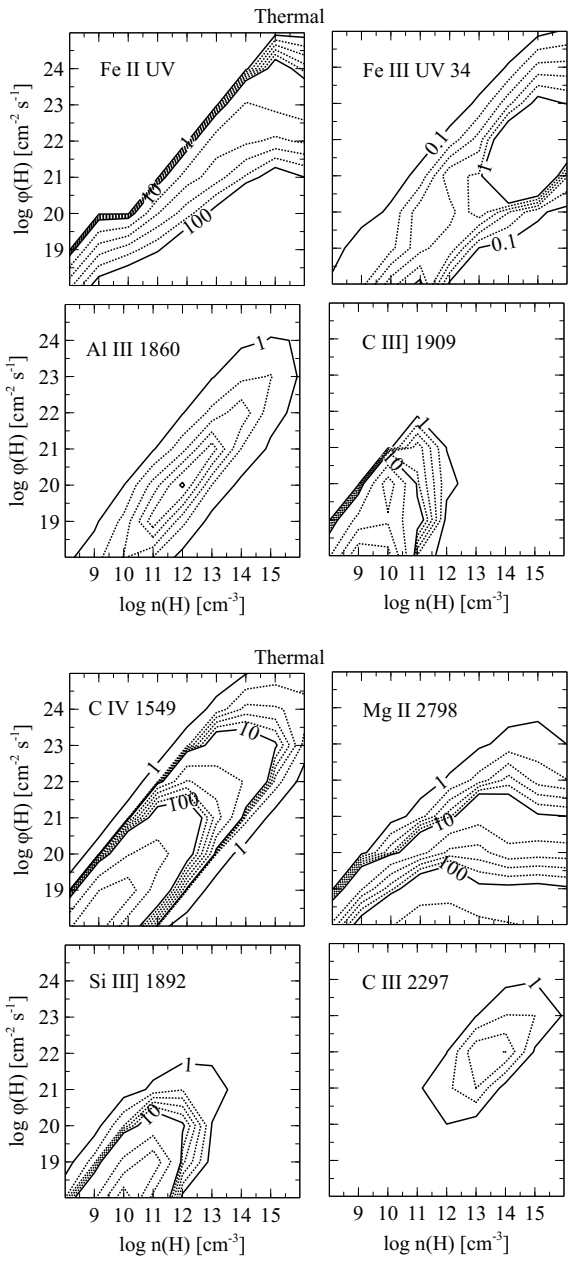

Figure 4. The ensemble of possible photoionization models for thermal line widths. Contours show the predicted equivalent widths in Ångströms relative to the continuum at 1215 Å for each emission feature, assuming a covering factor of unity. The integrated Fe II ultraviolet emission over the interval 2200-2660 Å is reported as a single feature.

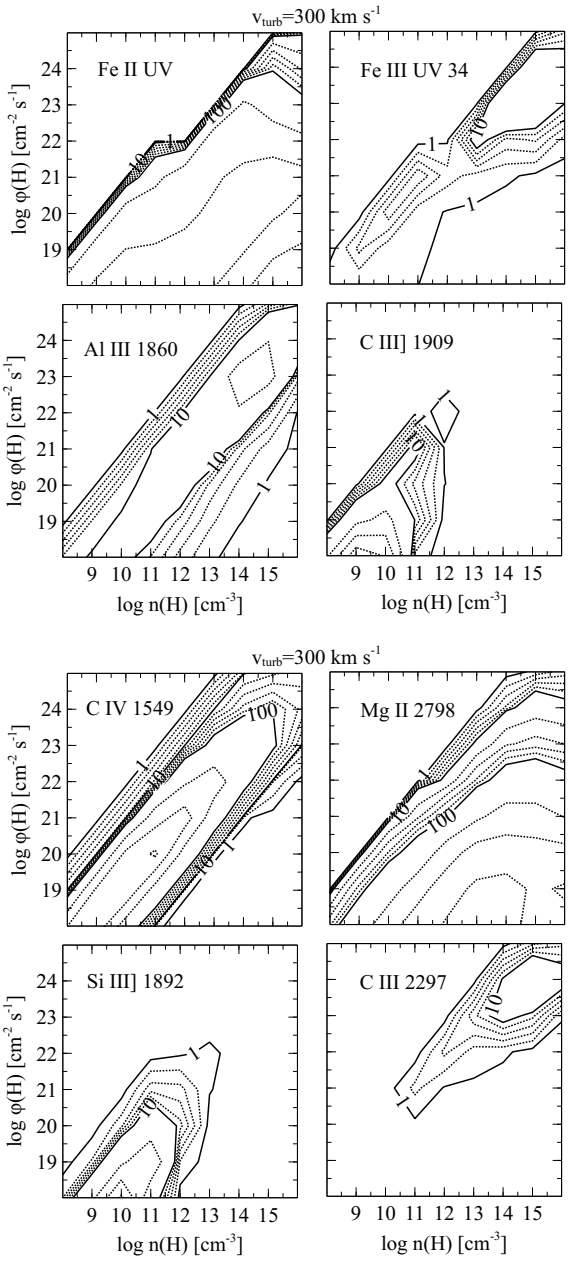

Figure 5. The ensemble of possible photoionization models, with microturbulence of 300 km s^{-1}. Contours show the predicted equivalent widths in Ångströms relative to the continuum at 1215 Å for each emission feature, assuming a covering factor of unity. The axes are identical to Fig. 4 and so the contours can be compared directly.

where $r_{73.6}$ is the radius in light days and we assume that the radiation field falls off as an inverse square law. Lower-ionization photoionized clouds that emit strongly in the ultraviolet and optical have kinetic temperatures in the neighbourhood of 1-2×10^4 K so the horizontal axis is an approximate surrogate for the gas pressure. We see that the source-cloud separation varies by nearly 4 dex while the gas pressure varies by 8 dex.

Intermediate ionization lines such as C IV and Al III peak along a diagonal corresponding to particular values of the ionization parameter

$$U = \frac{\phi(\mathrm{H})}{c\, n_H}. \quad (4)$$

Very low ionization lines such as Fe II and Mg II do not show such a peak but rather favour lower ϕ(H) and larger r.

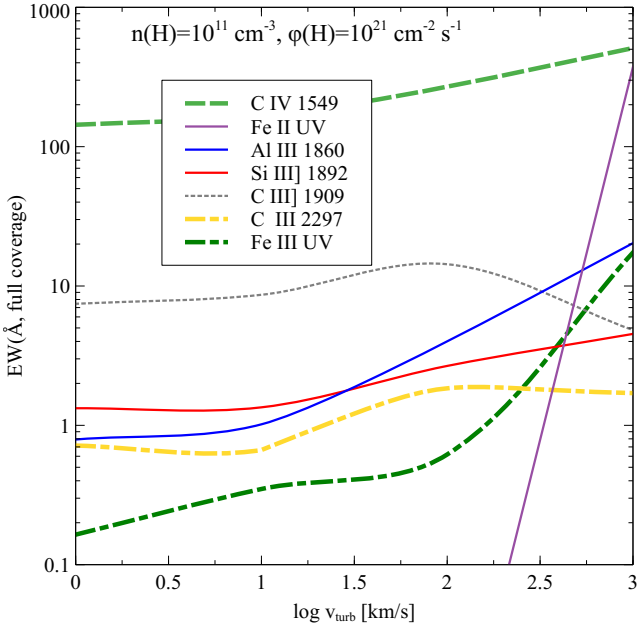

Figure 6. The effects of varying turbulence upon the equivalent widths of several prominent lines. Both Fe III and Fe II are predicted to produce much stronger emission as the turbulent velocity parameter increases.

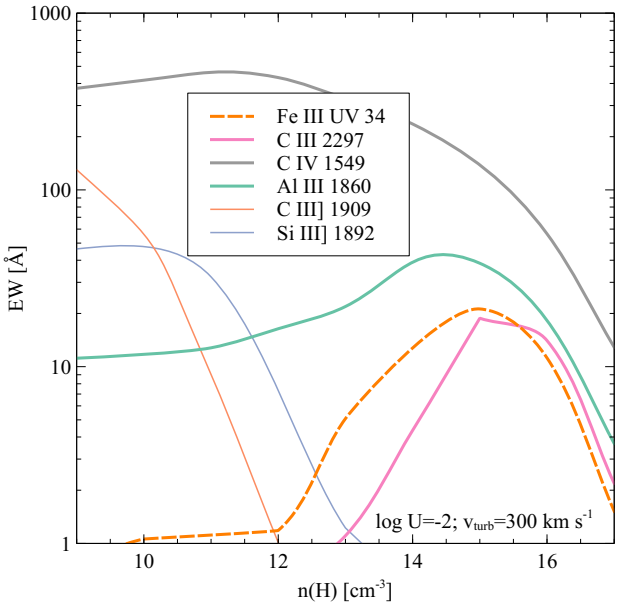

Figure 7. The effects of varying hydrogen density along the ridge of peak C IV emission strength, keeping the ionization parameter constant. C III] λ1909 and Si III] λ1892 produce very little emission above 10^{13} cm^{-3}, where both Fe III UV34 and Al III λ1860 are predicted to peak. C III λ2297 is predicted to be strong above 10^{14} cm^{-3}, but this line is not observed in quasar spectra.

4.2 Implications of the Fe III equivalent width; a turbulent dense medium

The energy level diagram shown in Figure 1 suggests that UV34 is an odd choice for the strongest Fe III line. The multiplet has a high excitation potential, with its upper level at 82 000 wavenumbers (10.2 eV). Direct excitation from the ground term is via forbidden transitions and so is not very efficient. Tests show that efficient excitation of UV34 is via a two-step process, with excited quintet levels playing an intermediary role.

Several Fe III levels are close enough to the Ly α energy of 82 259 wavenumbers for Ly α pumping to be significant. This is included in Cloudy as a general line excitation process and completes with direct continuum photoexcitation. Both processes will photoexcite the septets since these are connected to ground by an allowed electric dipole transition. However, the fact that the spectrum is sensitive to the turbulence, which affects continuum pumping more than line overlap, shows that continuum fluorescence is more important than Ly α pumping.

The effects of varying the turbulence are shown in Fig. 6. Increasing the turbulence increases the importance of continuum pumping because the line width increases and so do the number of continuum photons that can be absorbed by a transition (Section 2.1 of Ferland 1992). Physically, increased continuum pumping increases the population of excited quintets which can then undergo a collisional transition to the septets.

We note that, as discussed in Baldwin et al. (2004), the turbulence implemented in Cloudy describes any situation in which the wavelengths of the emitting lines are shifted or broadened over a physical distance corresponding to the mean free path of a continuum photon. Such velocity differences could naturally arise from differential rotation or instabilities within the accretion disc. We see no evidence for kinematic structure within the Fe III lines to suggest that the Fe III emitting material is itself outflowing, and so we do not believe that the turbulence needed to account for the observed strength of the Fe III emission is due to velocity gradients in ordered outflows as would be expected if the Fe III emitting material was entrained in a wind off the accretion disc.

Adopting a value of $v_{\rm turb} = 300\,{\rm km\,s^{-1}}$ for the microturbulence parameter, we find that the predicted equivalent width of Fe III emission is still significantly weaker than that observed in quasar spectra. Varying the metallicity of the emitting gas has an insufficient effect on the predicted equivalent width for the strength of Fe III in AGN to be explained by non-solar iron abundances. However, as shown in Figs. 4 and 5, the Fe III emission peaks at a density of $\simeq 10^{15}\,{\rm cm^{-3}}$, irrespective of the microturbulence. In Fig. 7, we show how the equivalent widths of various lines change as a function of density, taking a diagonal slice through the $\phi({\rm H}) - n_H$ plane corresponding to the ridge of peak C IV and Al III emission and constant ionization parameter.

The only way in which we can account for the observed strength of the Fe III emission is through turbulent, high density gas with $n_H > 10^{13}\,{\rm cm^{-3}}$. Taken with the upper limits on the density of the gas which is producing the semi-forbidden lines such as C III] λ1909 in quasar spectra, this is strong evidence for multiple components of differing densities contributing to the region which is producing the broad emission lines in AGN.

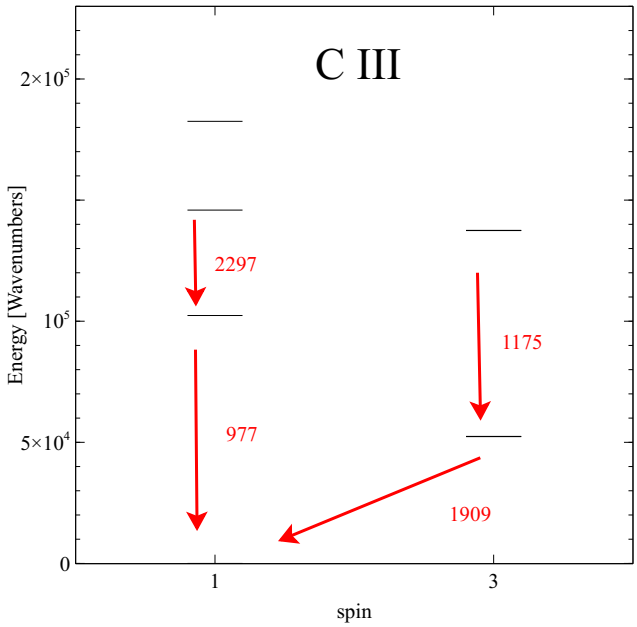

Figure 8. The C III model implemented in Cloudy. Only the lower levels are shown to keep the energy scale the same as Fig. 1. The strong C III lines are indicated.

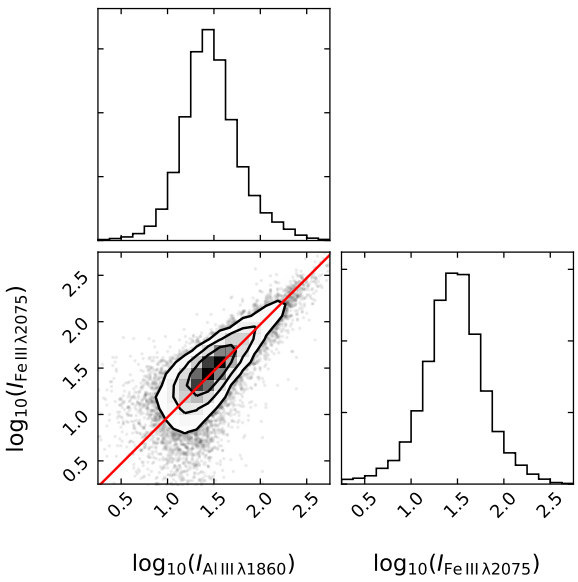

Figure 9. The observed intensities of the Al III doublet and Fe III λ2075 complex in units of 10^{-17} erg s^{-1} cm^{-2}. In red is the predicted ratio from the dense turbulent Cloudy model, which agrees very well with the slope of the observed correlation. The observed emission is consistent with the line ratio expected if both lines are produced in the same dense turbulent medium.

4.3 How dense is the turbulent dense medium?

In the previous subsection, we have shown that emission from a turbulent medium with density $n_H > 10^{13}$ cm^{-3} is required to reproduce the observed Fe III line strengths. To better constrain the density of this medium, we use the predicted strengths of the C III emission lines shown in Fig. 8.

As shown in Fig. 7, the strength of the semi-forbidden C III] λ1909 line drops drastically above $n_H \simeq 10^{12}$ cm^{-3}. We show in Section 5 that the C III] λ1909 emission in our sample of SDSS quasars is independent of the Fe III UV34 emission, consistent with emission from at least two distinct locations around the black hole.

The C III λ2297 line is predicted to be strong when the density is above $n_H \simeq 10^{14}$ cm^{-3} (Fig. 7). However, to the best of our knowledge, the line is not detected in the spectrum of any quasar. In particular, C III λ2297 is not present in the high signal-to-noise composites of Vanden Berk et al. (2001) and Francis et al. (1991), or the ultraviolet spectrum of I Zw 1 presented in Vestergaard & Wilkes (2001). We therefore use the observed lack of C III λ2297 emission to constrain the density of the Fe III emitting gas to lie in the range $n_H = 10^{13-14}$ cm^{-3}.

5 COMPARISON WITH OBSERVATIONS

With theoretical predictions from Cloudy in hand, we can now use the full sample of spectra described in Section 3.1 to test our preferred model for the dense turbulent medium required to reproduce the observed Fe III.

5.1 Measuring Fe III UV34 in quasar spectra

As shown in Figs. 6 and 7, the dense turbulent medium will also produce a significant amount of Al III doublet emission at $\lambda\lambda$1854.72,1862.79. For each of the 26 501 quasars in our sample, we fit the Al III doublet with two Gaussians, with the ratio of the lines constrained to be 2.3866 : 1.9162, and compare with the strength of the Fe III λ2075 complex described in Section 3.2. The results are shown in Fig. 9: the strength of the Al III doublet clearly correlates with the strength of the Fe III λ2075. The ratio of the line intensities of the two complexes is in agreement with the predictions of our dense turbulent model.

Encouraged by this, we fit the λ1909 complex with a model which describes the relative contribution of the aluminium, iron, carbon and silicon lines.

For each object, a power-law in flux is defined at 1800 and 2020 Å and subtracted from the spectrum. The wavelength region 1820-1920 Å is then fit with a sum of seven Gaussians described by four free parameters: (i) the amplitude of the Al III and Fe III UV34 component, (ii) the amplitude of the Si III] line, (iii) the amplitude of the C III] line, and (iv) the velocity width of the lines. The Al III doublet and Fe III UV34 triplet are constrained to have the line ratios

$$\lambda1854.72 : \lambda1862.79 : \lambda1895.46 : \lambda1914.06 : \lambda1926.30 = 2.3866 : 1.9162 : 0.9910 : 0.7538 : 0.6945 \quad (5)$$

as predicted for a dense, microturbulent, photoionized gas[1]

[1] $\nu = 300$ km s^{-1}, $n_H = 10^{14}$ cm^{-3}, $\phi = 10^{23}$ cm^{-2} s^{-1}

with solar abundances. In theory the Si III] and C III] lines would be expected to have narrower profiles than the Al III and Fe III, as they are coming from gas which is less dense and thus located further from the black hole. In practice the S/N of the spectra are such that allowing the velocity widths of the lines to vary independently leads to an over-fit to the data. We therefore constrain the velocity widths of all lines in our fitting routine to be equal, which gives a more robust estimate of the equivalent width of each line in the complex. Examples of our best fitting models are presented in Appendix C.

5.2 Implications for C III] and Si III]

The improved atomic data and CLOUDY model presented above now allow a more certain estimate of the UV34 multiplet to be made in any given quasar spectrum, even when the multiplet is completely blended with other lines. This allows, for the first time, an accurate measurement of the C III] and Si III] emission to be made in objects with a significant contribution from Fe III UV34.

Using our dense turbulent model for Fe III emission to fit the λ1909 complex, with independent contributions from Si III] and C III], we measure the equivalent widths of the Si III], C III] and Fe III lines in our sample of SDSS quasars. The results are shown in Fig. 10. We find that the Fe III emission correlates with the Si III], but that the C III] emission is essentially uncorrelated with either species. This is consistent with the expected behaviour of C III] λ1909, which must be coming from gas of a significantly lower density than that which is emitting the Fe III (see Section 4.3).

The Si III] strength does however correlate with the strength of the Fe III UV34, suggesting that some of the observed silicon emission could also be coming from the dense turbulent component. The observed C III]:Si III] ratio thus correlates with Fe III and could therefore be an indicator of the hardness of the SED which is illuminating the broad line region, as suggested by Casebeer et al. (2006) and Richards et al. (2011).

The median equivalent widths of emission in our sample are 2.58, 9.95, 5.97, and 4.43 Å for Fe III UV34, C III], Si III], and Al III respectively; the average strength of Fe III UV34 is ≈0.16 times the combined strength of C III] and Si III]. 83 per cent of the quasars in our sample have UV34 fluxes which are greater than 0.1 times the sum of flux in C III] and Si III]. This highlights the need for accurate modeling of UV34 when attempting to measure C III] and Si III] line properties.

5.3 Broad absorption line quasars

The absorption line properties of the 19 590 quasars in our sample with $z > 1.56$, where spectral coverage of the C IV emission line is available, are classified as part of the Rankine et al. (2020) investigation into broad absorption line (BAL) quasars. The classification of objects as BAL quasars from this subsample produces 16 148 non-BAL and 3048 high-ionization BAL quasars. We exclude 394 low-ionization BALs with broad Al III troughs from subsequent analysis.

Following the same scheme as described above, we find no significant difference between the high-ionization BALs and non-BALs, in that the high-ionization BALs also require a high density, turbulent component to account for the Fe III emission in their spectra.

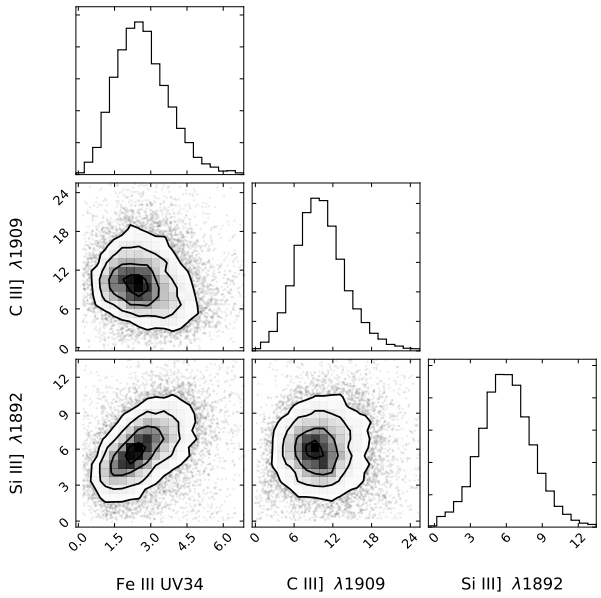

Figure 10. Observed equivalent widths in Ångströms for three components of the λ1909 complex, relative to the continuum at 1900 Å. When the Fe III UV34 emission is incorporated into the fit to the complex, we find that the C III] emission strength is uncorrelated with that of Si III].

5.4 Comparison with Vestergaard & Wilkes (2001)

In this section we compare our Fe III UV34 multiplet with those presented in the templates of Vestergaard & Wilkes (2001).

Vestergaard & Wilkes (2001) discuss the blending of UV34 with the C III] and Si III] lines and the degeneracies arising when attempting to fit multiple overlapping lines simultaneously due to the non-orthogonality of Guassian functions (their section 5.1). Due to the lack of atomic data at the time, they were unable to place theoretical constraints on the UV34 line ratios and thus provided a range of ratios which were consistent with the observed emission. Their published ratios range from the optically thick case where the lines thermalise at 1:1:1, to their preferred values of 0.375:1:0.425 based on the observed strength of the λ1914 line in I Zw 1.

Using the new atomic data and the dense turbulent CLOUDY model presented above, we are now able to predict the ratios of the $\lambda\lambda$1895.46,1914.06,1926.30 Fe III lines in quasar spectra. Assuming a dense, microturbulent, photoionized gas with solar abundances, we find UV34 line ratios of 1.316:1:0.921.

Our preferred Fe III model therefore predicts stronger λ1895 emission relative to λ1914 than any of the models presented by Vestergaard & Wilkes (2001), but we believe our line ratios are still consistent with those they observe in I Zw 1 within the uncertainties they discuss.

6 DISCUSSION

6.1 High Densities

It is perhaps surprising to see that significant line emission from Fe III and Al III is predicted from gas illuminated by such high ionizing fluxes. Our favoured model for the Fe III emitting gas has an ionizing photon flux $\phi = 10^{23}\,\mathrm{cm}^{-2}\,\mathrm{s}^{-1}$, which suggests that this part of the BLR must lie very close to the central black hole. While this is consistent with the existing reverberation-mapping studies in the literature (see Section 1), we would expect this locale to have large Keplerian speeds - the 4 dex difference in ϕ gives a 2 dex difference in radius and hence v_{Kepler} a factor 10 greater compared to the gas which is most likely emitting C III].

We would expect such an extreme difference in the velocity width of the emission lines to be easily observable, however, no such difference is seen in the objects in our sample. The spectral resolution and S/N constraints are such that, while we cannot rule out variation between the velocity widths of each species within individual objects at the level of tens of per cent, the Si III] and C III] lines are no more than a factor 2 narrower than the Al III lines in any given object in our sample.

One explanation for this is if the dense turbulent gas which is emitting Fe III is primarily undergoing equatorial motion. For a Type-1 quasar, this would mean that the majority of the motion of the line emitting gas is in the plane of the sky, and the observed velocity dispersion along the line of sight is smaller than the Keplerian speed. This would suggest that the dense media we require to explain the strength of the observed Fe III emission are found in quasi-ordered flows in the equatorial regions of the AGN.

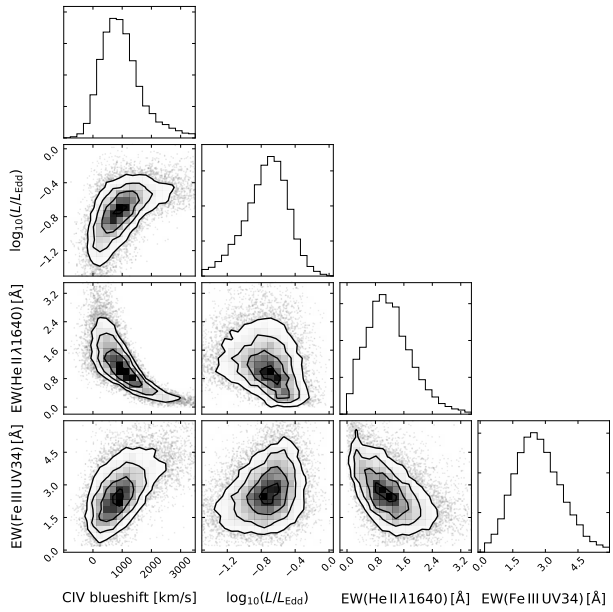

Figure 11. The equivalent width of Fe III UV34 emission, shown against the observed blueshift of the C IV emission line (as defined in Rankine et al. 2020), the Eddington ratio, and the equivalent width of He II λ1640 emission. The strength of Fe III increases with the signature of stronger nuclear outflows, which might be driven by higher L/L_{Edd}. However, the strengths of Fe III and He II anticorrelate, suggesting that the link between Fe III and C IV could also be driven by variation in the SED which is illuminating the BLR.

6.2 Correlations with C IV properties

The high-ionization C IV λ1549 emission line exhibits a large range of kinematic morphologies, from strong, 'peaky' emission at the systemic redshift which is believed to be dominated by emission from gas in virial equilibrium, to weaker and highly blueshifted emission tracing outflowing material. However, the physical mechanisms which set the balance of these emitting components are not well understood, despite the fact that the C IV morphology is known to be closely tied to other parameters such as the Eddington ratio and the hardness of the SED which is ionizing the BLR (Richards et al. 2011; Rankine et al. 2020). Here we note certain correlations using the results of the modelling of the λ1909 complex described in Section 5.

The measured strength of the Fe III and Al III component tends to increase as the blueshift of the C IV line increases (Fig. 11), suggesting that objects with stronger wind emission are likely to display stronger emission from the dense turbulent medium. This is consistent with the results from the sample of seven objects studied by Baldwin et al. (1996). However, the Fe III line profiles do not themselves show any evidence for outflows, and so we do not believe that the dense ($\simeq 10^{14}\,\mathrm{cm}^{-3}$) Fe III emitting gas is being accelerated within a wind.

One possible explanation for the correlation between the strength of the Fe III UV34 emission and the increasing blueshifted C IV emission, tracing outflowing lower density material, might be the range of Eddington fractions within the population, which is one of the commonly quoted drivers of variation in C IV line properties. Quasars with larger Eddington fractions potentially 'puff up' the inner regions of the accretion disc (e.g. Giustini & Proga 2019), leading to a larger volume of high density line emitting gas close in to the black hole. The increased Eddington fraction also leads to stronger radiation line-driven winds. However, inferring L/L_{Edd} from single-epoch spectra is fraught with large systematic uncertainties, deriving both from the use of a single bolometric correction to estimate L_{bol} from a monochromatic luminosity, and also the use of a virial factor to estimate the black hole mass from a single emission line velocity width. Here we use the FWHM of the Mg II λ2800 line and the single-epoch virial estimator described by Vestergaard & Osmer (2009) to estimate black hole masses, and the monochromatic luminosity at 3000 Å to estimate L_{bol} and hence L/L_{Edd}. This quantity is also shown in Figure 11, along with the observed equivalent width of the He II λ1640 emission line.

As expected, we recover the correlation between L/L_{Edd} and C IV blueshift. We also find that objects with stronger Fe III emission tend to have higher L/L_{Edd} ratios, consistent with the scenario outlined above. However, not all objects with high L/L_{Edd} display strong Fe III emission, suggesting that L/L_{Edd} is not the sole driver of the Fe III equivalent width.

On the other hand, we also find that the equivalent width of UV34 anticorrelates with that of He II λ1640, which

is another quantity known to show strong trends with C IV line properties. He II is believed to trace the hardness of the SED which is illuminating the BLR, i.e. the strength of the extreme ultraviolet continuum radiation which is largely unseen by the observer. The observed correlation between Fe III and C IV could thus be driven by changes in the shape of the ionising SED. However, recent work by Ferland et al. (2020) has also pointed out that changes in the equivalent width of He II are also expected due to changes in the covering factor of the He II emitting gas, which could itself be varying in response to the hardness of the unseen SED, and thus the equivalent width of He II may not enjoy a linear relationship with the relative flux of Helium-ionising photons.

7 CONCLUSIONS

While Fe III has long been known to be present in AGN spectra, the recent large set of atomic data of Badnell & Ballance (2014) makes theoretical predictions of its emission spectrum possible for the first time.

Using CLOUDY, we have computed predictions for the strength of the Fe III emission across a large range of parameter space, exploring the effect of variations in the density, ionizing flux and turbulence of the emitting gas. The highly-excited UV34 multiplet is predicted to be the strongest feature, and the new predictions allow this multiplet to be accurately subtracted from the 1909 Å C III] + Fe III + Si III] complex. Our main results are as follows:

- The lack of observed Fe III emission below 1000 Å shows that the Fe III lines in AGN are emitted by photoionized gas.
- Strong Fe III UV34 emission in quasar spectra demonstrates that high density ($n_H \simeq 10^{14}\,\mathrm{cm}^{-3}$) gas is present in the majority of luminous quasars. This gas must also produce large amounts of Al III $\lambda\lambda$1855,1863.
- Together with the upper bounds on density from semi-forbidden lines such as C III], our results show that the broad line region in AGN must have a non-uniform density structure. Our analysis suggests that the Fe III emission originates in gas about 1 dex closer to the black hole than the source of C IV emission.
- Thermal line widths cannot produce sufficiently strong Fe III emission. Non-thermal line widths must therefore be present to increase the equivalent width by continuum pumping, i.e. increasing the number of continuum photons which can excite the transition.
- Baldwin et al. (2004) found that microturbulence also improves the fit to the Fe II spectrum. Fe III is a more straightforward case since its spectrum is much simpler with isolated lines. Together, the strength of the Fe II and Fe III emission in quasar spectra make a compelling case for a turbulence in the line emitting region.
- Using the new atomic data, and our dense turbulent model, it is possible to predict the line ratios in the Fe III UV34 multiplet: λ1895.46 : λ1914.06 : λ1926.30 = 1.316 : 1 : 0.921.
- Using the observed strength of the Al III doublet, the Fe III UV34 multiplet can be modelled and subtracted from the 1909 Å complex (equation 5). This enables a more accurate measurement of the C III] and Si III] emission, even when these lines are blended together.

ACKNOWLEDGEMENTS

We thank the anonymous referee for a thoughtful report which led to improved clarity in many parts of the manuscript. It is a pleasure to note useful comments from Bob Carswell, Gordon Richards, and Hagai Netzer. MJT and ALR thank the Science and Technology Facilities Council (STFC) for the award of studentships. GJF acknowledges support by NSF (1816537), NASA (ATP 17-ATP17-0141), and STScI (HST-AR-15018). PCH acknowledges funding from STFC via the Institute of Astronomy, Cambridge, Consolidated Grant. CPB acknowledges support through R1711APL : QUB Astronomy Observation and Theory Consolidated Grant. NRB is funded by STFC Grant ST/R000743/1 with the University of Strathclyde. This work made use of Astropy (Astropy Collaboration et al. 2013; Price-Whelan et al. 2018), Matplotlib (Hunter 2007), and corner.py (Foreman-Mackey 2016).

Funding for the Sloan Digital Sky Survey IV has been provided by the Alfred P. Sloan Foundation, the U.S. Department of Energy Office of Science, and the Participating Institutions. SDSS-IV acknowledges support and resources from the Center for High-Performance Computing at the University of Utah. The SDSS web site is www.sdss.org.

SDSS-IV is managed by the Astrophysical Research Consortium for the Participating Institutions of the SDSS Collaboration including the Brazilian Participation Group, the Carnegie Institution for Science, Carnegie Mellon University, the Chilean Participation Group, the French Participation Group, Harvard-Smithsonian Center for Astrophysics, Instituto de Astrofísica de Canarias, The Johns Hopkins University, Kavli Institute for the Physics and Mathematics of the Universe (IPMU) / University of Tokyo, the Korean Participation Group, Lawrence Berkeley National Laboratory, Leibniz Institut für Astrophysik Potsdam (AIP), Max-Planck-Institut für Astronomie (MPIA Heidelberg), Max-Planck-Institut für Astrophysik (MPA Garching), Max-Planck-Institut für Extraterrestrische Physik (MPE), National Astronomical Observatories of China, New Mexico State University, New York University, University of Notre Dame, Observatário Nacional / MCTI, The Ohio State University, Pennsylvania State University, Shanghai Astronomical Observatory, United Kingdom Participation Group, Universidad Nacional Autónoma de México, University of Arizona, University of Colorado Boulder, University of Oxford, University of Portsmouth, University of Utah, University of Virginia, University of Washington, University of Wisconsin, Vanderbilt University, and Yale University.

REFERENCES

Astropy Collaboration et al., 2013, A&A, 558, A33
Badnell N. R., Ballance C. P., 2014, ApJ, 785, 99
Baldwin J., Ferland G., Korista K., Verner D., 1995, ApJ, 455, L119+
Baldwin J. A., et al., 1996, ApJ, 461, 664
Baldwin J. A., Ferland G. J., Korista K. T., Hamann F., LaCluyzé A., 2004, ApJ, 615, 610
Boroson T. A., Green R. F., 1992, ApJS, 80, 109
Bottorff M., Ferland G., Baldwin J., Korista K., 2000, ApJ, 542, 644
Casebeer D. A., Leighly K. M., Baron E., 2006, ApJ, 637, 157
Ferland G. J., 1992, ApJ, 389, L63

Ferland G. J., et al., 2017, Rev. Mex. Astron. Astrofis., 53, 385
Ferland G. J., Done C., Jin C., Landt H., Ward M. J., 2020, MNRAS,
Fian C., Guerras E., Mediavilla E., Jiménez-Vicente J., Muñoz J. A., Falco E. E., Motta V., Hanslmeier A., 2018, ApJ, 859, 50
Foreman-Mackey D., 2016, The Journal of Open Source Software, 24
Francis P. J., Hewett P. C., Foltz C. B., Chaffee F. H., Weymann R. J., Morris S. L., 1991, ApJ, 373, 465
Giustini M., Proga D., 2019, A&A, 630, A94
Graham M. J., Clowes R. G., Campusano L. E., 1996, MNRAS, 279, 1349
Grier C. J., et al., 2019, ApJ, 887, 38
Hu C., et al., 2015, ApJ, 804, 138
Hunter J. D., 2007, Computing In Science & Engineering, 9, 90
Jin C., Ward M., Done C., 2012, MNRAS, 425, 907
Korista K., Baldwin J., Ferland G., Verner D., 1997, ApJS, 108, 401
Kramida A., Yu. Ralchenko Reader J., and NIST ASD Team 2018, NIST Atomic Spectra Database (ver. 5.6.1), [Online]. Available: `https://physics.nist.gov/asd` [2019, September 6]. National Institute of Standards and Technology, Gaithersburg, MD.
Laha S., Tyndall N. B., Keenan F. P., Ballance C. P., Ramsbottom C. A., Ferland G. J., Hibbert A., 2017, ApJ, 841, 3
Lykins M. L., Ferland G. J., Porter R. L., van Hoof P. A. M., Williams R. J. R., Gnat O., 2013, MNRAS, 429, 3133
Lykins M. L., et al., 2015, ApJ, 807, 118
Marziani P., Sulentic J. W., 2014, MNRAS, 442, 1211
Mediavilla E., Jiménez-Vicente J., Fian C., Muñoz J. A., Falco E., Motta V., Guerras E., 2018, ApJ, 862, 104
Mediavilla E., Jiménez-Vicente J., Mejía-Restrepo J., Motta V., Falco E., Muñoz J. A., Fian C., Guerras E., 2019, ApJ, 880, 96
Moore C. E., 1952, An ultraviolet multiplet table
Nikolić D., et al., 2018, ApJS, 237, 41
Osterbrock D. E., Ferland G. J., 2006, Astrophysics of gaseous nebulae and active galactic nuclei
Pâris I., et al., 2017, A&A, 597, A79
Pâris I., et al., 2018, A&A, 613, A51
Price-Whelan A. M., et al., 2018, AJ, 156, 123
Rankine A. L., Hewett P. C., Banerji M., Richards G. T., 2020, MNRAS, 492, 4553
Richards G. T., et al., 2011, AJ, 141, 167
Shen Y., et al., 2011, ApJS, 194, 45
Stevans M. L., Shull J. M., Danforth C. W., Tilton E. M., 2014, ApJ, 794, 75
Vanden Berk D. E., et al., 2001, AJ, 122, 549
Vestergaard M., Osmer P. S., 2009, ApJ, 699, 800
Vestergaard M., Wilkes B. J., 2001, ApJS, 134, 1
Wills B. J., Netzer H., Wills D., 1985, ApJ, 288, 94
Zhang Z.-X., et al., 2019, ApJ, 876, 49

APPENDIX A: ATOMIC DATA SOURCES

Version 17 of Cloudy obtains most of its atomic data from external data files (Ferland et al. 2017). Our "Stout" data format is described in Lykins et al. (2015). This structure makes it simple to "drop in" large data sets such as the Fe III data presented in Badnell & Ballance (2014). Those data were published in ADF04 format, a common structure used for atomic data exchange, and the Cloudy project has scripts to convert ADF04 to our Stout format.

High densities are considered in this investigation. Ferland et al. (2017) describes our "equivalent two-level atom" model used to derive the ionization of many-electron systems. This works in terms of total summed recombination rate coefficients. Recombination processes are suppressed at high densities and our approach in treating this process is described in Nikolić et al. (2018). This physics is highly uncertain and we have experimented by changing the suppression factor by ±0.5 dex. The conclusions reached in this paper were unchanged.

APPENDIX B: SYSTEMIC REDSHIFT ESTIMATION

The systemic redshifts used in this work are those described by Rankine et al. (2020), which do not make use of the C IV line. This approach avoids biasing the systemic redshift estimation in cases where the C IV emission profile is skewed, which we have found to be an issue with the SDSS pipeline redshifts. Using our redshifts, and the Fe III energy level data now included in Cloudy, we find that the Fe III emission in our sample is consistent with coming from gas at the systemic redshift. In particular, we are unable to reproduce the result of Mediavilla et al. (2018), who find that the Fe III λ2075 emission lines are systematically redshifted, and the magnitude of this additional redshift is correlated with the full width at half maximum (FWHM) of the C IV emission line.

In Fig. B1, we show composite spectra constructed from those objects in our sample which are also contained within the twelfth data release of the SDSS, of which the quasar catalogue (Pâris et al. 2017) reports the FWHM of the Mg II emission line. We construct two composites: one using 375 objects with FWHM(Mg II) in the range 2000-4000 $\mathrm{km\,s^{-1}}$, and one using 967 objects with FWHM(Mg II) in the range 9000-15 000 $\mathrm{km\,s^{-1}}$. The median FWHM(Mg II) in each subsample is 3800 and 10 200 $\mathrm{km\,s^{-1}}$ respectively. The narrow-lined composite is artificially broadened using a Gaussian kernel to match the velocity width of the broader-lined subsample. The work of Mediavilla et al. (2019, their Fig. 2) would suggest that the factor of ≃2.7 difference in FWHM(Mg II) would correspond to a shift of at least 10 Å in the location of the Fe III lines between the two composites, which we would expect to be easily detectable. We see that the peak of Mg II is observed at 2798 Å in both our composites, and there is no noticable difference between the peak of the Fe III complex marked at 2073.5 Å.

APPENDIX C: MODELLING THE 1909 Å COMPLEX

In Fig. C1, we present six examples of our best fitting models for the 1909 Å emission complex, as described in Section 5. Each model is fit to the data in the wavelength range 1820-1920 Å, avoiding contamination from weak Fe II emission features at ≃1940 Å.

This paper has been typeset from a TEX/LATEX file prepared by the author.

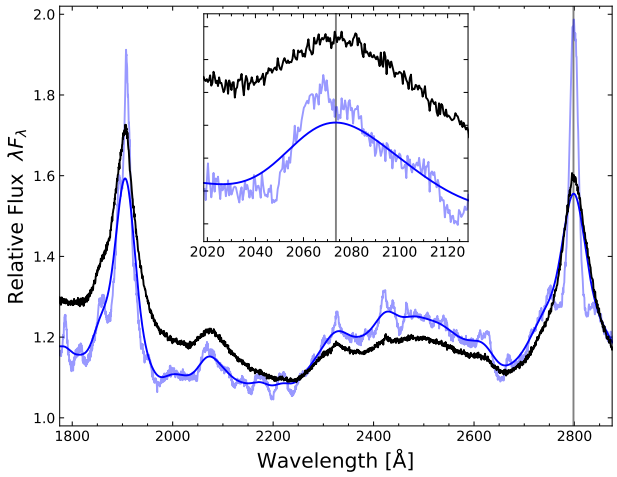

Figure B1. Composite of objects in our sample with FWHM(Mg II) $\simeq$3800 km s^{-1} (blue) and $\simeq$10 200 km s^{-1} (black). The narrow-lined composite has been broadened with a Gaussian kernel to match the velocity widths. Inset: the location of peak of the Fe III complex is seen at at 2073.5 Å both composites.

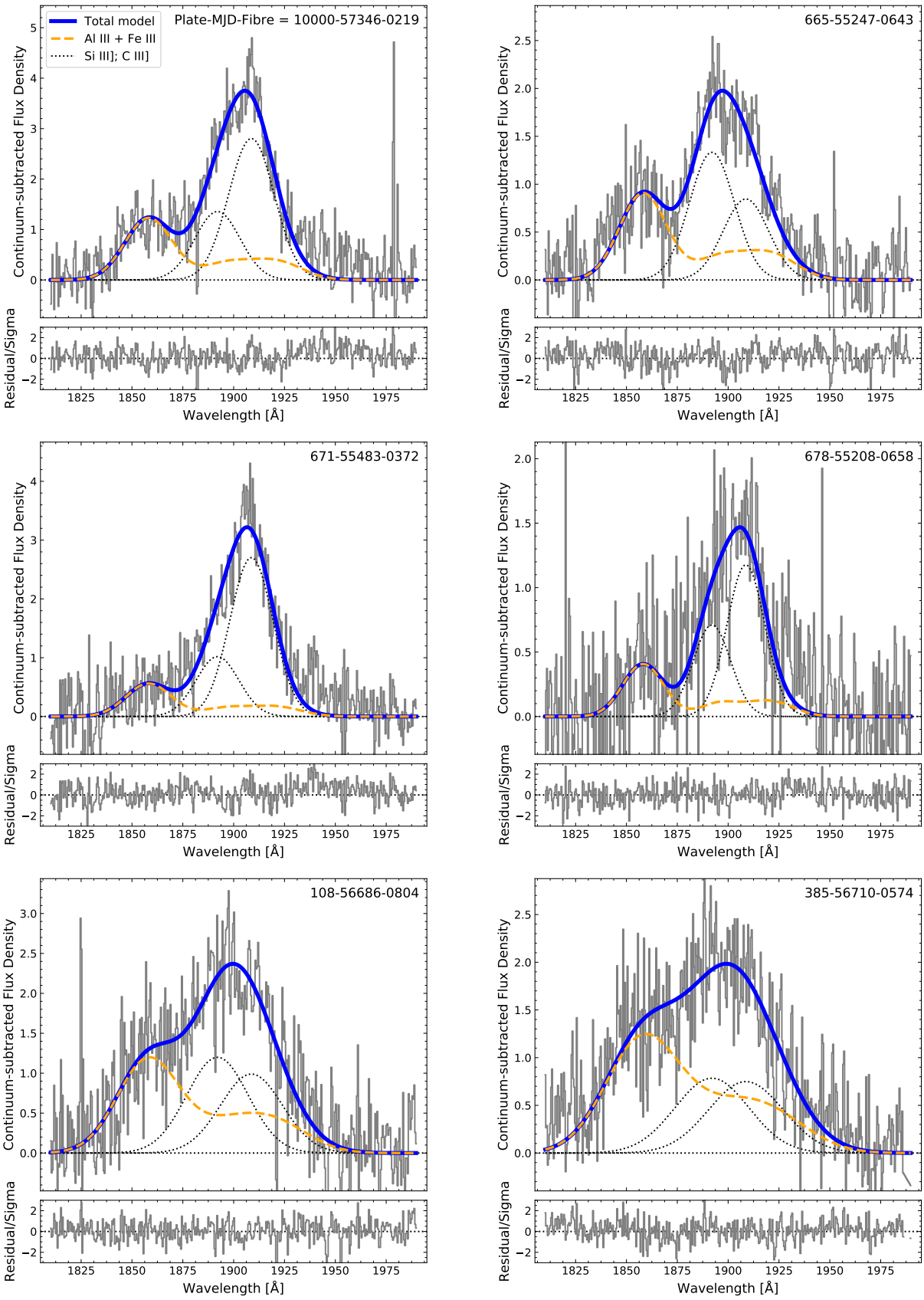

Figure C1. Examples of our best fitting models to the 1909 Å complex. The C III] emission may be slightly narrower than the Al III and Fe III emission in e.g. 671-55483-0372, but in general the S/N is such that constraining the velocity widths of all lines to be equal provides a reasonable fit to the data.